Elastic constants of cubic boron phosphide and boron arsenide

Sushant Mahat, Sheng Li, Hanlin Wu, Pawan Koirala, Bing Lv, and David G. Cahill

Phys. Rev. Materials **5**, 033606 — Published 16 March 2021

DOI: 10.1103/PhysRevMaterials.5.033606

Elastic constants of cubic boron phosphide and boron arsenide

Sushant Mahat,[1,*] Sheng Li,[2] Hanlin Wu,[2] Pawan Koirala,[2] Bing Lv,[2] and David G. Cahill[1]

[1]Department of Materials Science and Engineering and Materials Research Laboratory, University of Illinois at Urbana-Champaign, Urbana, IL 61801

[2]Department of Physics, The University of Texas at Dallas, Richardson, TX 75080

We report the room temperature elastic constants of boron phosphide and boron arsenide single crystals derived from Brillouin frequencies measured by picosecond interferometry. The synthesis of BP and BAs with thermal conductivity as high as 540 and 1000 $Wm^{-1}K^{-1}$, respectively, has made them into promising materials for thermal management. Accurate measurements of elastic constants are needed to assess the accuracy of computational modeling of the lattice dynamics. The crystals are cut and polished in different orientations to access waves travelling along different directions. The surface normal orientations of the crystals are determined using electron backscattering diffraction. We studied the Brillouin frequencies of quasi longitudinal waves in five different orientations of BP and BAs crystals. Quasi shear waves were observed in two orientations of BP and one orientation of BAs. The propagation directions and acoustic velocities are used to construct Christoffel equations which are then solved for the elastic constants. We report C_{11}, C_{12}, and C_{44} values of 354 ± 5 GPa, 83 ± 15 GPa, and 190 ± 8 GPa for BP and 291 ± 5 GPa, 76 ± 13 GPa, and 173 ± 6 GPa for BAs. The measured elastic constants for BAs differ by less than 5 % and 17 % from calculated elastic constants obtained through local density approximation (LDA) and Perdew-Burke-Ernzerhof (PBE) density functional calculations, respectively. In most cases, the measured elastic constants are larger than the calculated elastic constants.

I. Introduction

[*]smahat2@illinois.edu

Thermal management of hot spots is a growing problem in microelectronic devices [1,2]. The primary mode of heat transfer internal to a chip module is by conduction where a high thermal conductivity material conducts heat from the high power electronic device to a larger heat exchanger [3]. New materials with high thermal conductivity are therefore of significant interest for their use as heat spreading materials. Lindsay *et al.* [4] implemented recently developed *ab initio* calculations for thermal transport to predict high room temperature thermal conductivity Λ in cubic III-V boron compounds. Following their prediction, boron phosphide and boron arsenide with high thermal conductivity Λ of 540 and 1000 W/m-K respectively have been synthesized, making them candidates for applications in thermal management [5–7].

In a first principles approach, Λ values are determined using inter-atomic force constants (IFCs) calculated through density functional theory (DFT). IFCs are used to derive properties such as phonon frequencies, velocities, and lifetimes, which in turn determine Λ [8]. The accuracy of the DFT calculation of IFCs depends on the choice of the exchange correlation (XC) energy functional. Råsander et al. [9] compared theoretical and experimental elastic constants in 18 semiconductors and reported varying degrees of errors in elastic constants depending on the choice of the XC energy functional. Comparing elastic constant measurements with elastic constants calculated using different XC energy functionals can therefore help quantify the accuracy of DFT calculations in determining IFCs and thus in determining Λ of materials [9].

Elastic constants of BP have been experimentally determined using Brillouin scattering and the bulk modulus has been measured for both polycrystalline and single crystal BP samples using *in situ* X-ray diffraction in a diamond anvil cell [10,11]. These previous publications agree on a relatively high bulk modulus of approximately 174 GPa for BP. However, the BP material used in the prior Brillouin scattering experiment was an epitaxial layer grown on a Si (100) substrate by chemical vapor

deposition [10,12]. Epitaxial layers grown in this manner were of uncertain quality and were expected to have lattice imperfections and Si impurities [12].

For BAs, measurements of the bulk modulus of polycrystalline samples under the application of hydrostatic pressure in a diamond anvil cell have been carried out [13,14]. The propagation of surface acoustic waves on the (111) surface of BAs crystals and the propagation of longitudinal acoustic waves normal to the (111) have also been investigated using picosecond acoustics [15]. The three elastic constants of BAs have been derived from these various experiments [15]. Here, we provide a new and more direct measurement of all three elastic constants of BP and BAs crystals using a single method.

We determined the elastic constants of cubic BP and BAs crystals from acoustic velocities v along different propagation directions in the crystals. In a material with density ρ, $v^2 = C_{eff}/\rho$, where the effective elastic modulus C_{eff} can be expressed as a function of the elastic constants of a material, the polarization of the elastic wave, and the direction cosines for the direction of propagation of the elastic wave. For example, the effective elastic modulus C_{eff} in cubic crystals for a longitudinal wave propagating in the [111] direction is 1/3 (C_{11}+2C_{12}+4C_{44}). For an arbitrary direction, a more elegant treatment involves defining a Christoffel tensor that describes the solution to any elastic waves for a given direction and polarization [16,17]. In cubic crystals such as BP and BAs, there are three independent elastic constants; measuring acoustic velocities and solving related Christoffel equations in any three unique propagation directions or polarizations is, in principle, sufficient to determine the three elastic constants. Longitudinal velocities however only have a weak dependence on C_{12} and C_{44} independently; therefore, in practice at least one transverse velocity measurement is also necessary [18]. However, the size and shape of available single crystals can make it challenging to access these unique directions and polarizations.

In our experiment, we used picosecond interferometry (PI) combined with measurements of the index of refraction to measure acoustic wave velocities *v*. PI is a member of a broader set of picosecond ultrasonics technique which rely on optical pulses to generate and detect acoustic waves [19]. The use of optical pulses, which can be easily focused down to micrometer sizes, makes picosecond ultrasonics techniques better suited at measuring small samples than conventional techniques which require specific sample geometries and bulky transducers [20].

In the PI technique, a semitransparent thin metallic transducer layer is deposited on the sample, and acoustic waves are thermally generated by exciting a spot on this layer with pump pulses. The waves produced are usually limited to travelling in a direction perpendicular to the surface of the crystal. This poses a significant experimental problem for using PI to measure all three elastic constants in high quality BP and BAs crystals as the preferred orientation of the growth facets is [111] and consequently the only easily accessible surfaces are (111). This is reflected in the work of Kang *et al.* [15] where all velocity measurements were done on the (111) plane of BAs crystals. In our work, we overcame this problem by cutting the crystals along different directions to expose new facets which allowed us access to different propagation directions. The orientations of the exposed facets were determined through electron backscattering diffraction (EBSD).

II. Experimental Details

A. Sample preparation: BP crystals were grown by a modified flux method using copper phosphide as the flux [5]. BAs crystals were grown through chemical vapor transport method described in previous publications [6,21]. Most of the crystals used were smaller than 0.5 mm^3, and irregularly shaped. We therefore embedded the crystals in epoxy to facilitate easier handling and polishing. Cuboid sections containing the crystals were cut from the larger epoxy body. These cuboid structures were polished

using 15-micron grade diamond lapping films until a 200 – 400 μm length scale area of the embedded crystal was exposed.

The exposed faces were then polished using finer diamond lapping films (9, 3, 1, 0.1-micron grade). All polishing was done using an Allied MultiPrep^{TM} tool with each step involving between 2 to 5 minutes of polishing. The samples were monitored using a light microscope in between the polishing steps to ensure no visible scratches were introduced during the polishing process. De-ionized (DI) water was used as polishing fluid and the sample was cleaned between subsequent lapping film steps by submerging in ultrasonically activated DI water. A final vibratory polishing step lasting two hours using colloidal silica (0.02 μm) was employed to obtain the surface finish required for EBSD and PI measurements.

Five crystals each of BP and BAs were prepared in this manner. A <100> Si wafer was embedded in epoxy and sectioned and polished in a similar fashion to create four Si samples with different orientations embedded in cuboid epoxy structures. We measured the elastic constants of Si using these samples to validate our experimental approach.

B. Refractive index measurement: Each of the prepared BP and BAs samples were mounted on a rotational stage and a 778 nm beam was focused onto the crystals using a 5x objective lens ($1/e^2$ intensity radius of 10.6 μm). A three-axis translation stage was used to center the sample relative to the rotational stage. A polarizing beam splitter was used to obtain a p-polarized beam which was then focused on the polished crystal surface. The intensity of the reflected beam was measured using a power meter placed 5 cm from the crystal surface.

This setup allowed for the measurement of reflectance *R* of the beam for different angles of sample rotation θ_S as measured by the rotational stage. The angle of incidence θ and the sample rotation θ_S had a systematic offset (Δθ). θ_S values with the lowest reflectance (i.e., θ_S corresponding to Brewster's angle)

in both the counterclockwise and clockwise directions were found and $R(\theta_S)$ near these Brewster's angles were measured. Measuring $R(\theta_S)$ on both directions is required to solve for the offset $\Delta\theta$ between angle of sample rotation and angle of incidence.

From Fresnel's equations, the reflectance of a p-polarized beam can be calculated as [22]

$$R(\theta) = \left[\frac{\tan(\theta-\theta_t)}{\tan(\theta+\theta_t)}\right]^2, \quad (1)$$

where the angle of transmission θ_t can be related to the incidence angle θ and refractive index n using Snell's law. $R(\theta)$ values were calculated using eqn. 1 for a range of refractive indices n. Similarly, sets of experimental $R(\theta)$ were generated by shifting $R(\theta_S)$ using different possibilities of $\Delta\theta$. Each pair of computed and experimental $R(\theta)$ datasets were compared against each other to calculate absolute differences $|\Delta R(\theta)|$, which were averaged over for all θ points available to calculate the average sum of absolute differences $\langle\Sigma_{\Delta R}\rangle$ between the computed and experimental dataset. The combination of refractive index n and $\Delta\theta$ that produced the pair of datasets with the lowest $\langle\Sigma_{\Delta R}\rangle$ was selected as the best solution.

The standard deviation σ in $|\Delta R(\theta)|$ values for the pair of computed and experimental dataset leading to the best solution was then used to calculate the standard error ($\sigma/\sqrt{N}$, where N is total number of reflectance data points taken) in $\langle\Sigma_{\Delta R}\rangle$. Any refractive index and $\Delta\theta$ combination with a $\langle\Sigma_{\Delta R}\rangle$ value within this standard error of lowest $\langle\Sigma_{\Delta R}\rangle$ was a possible solution, which allowed for the calculation of uncertainty in refractive index (see fig. S1 in the Supplemental Material [23]). The uncertainty in all our refractive index measurements were approximately 2 %.

We also measured the refractive index of a Si wafer using this approach.

C. Electron backscattering diffraction (EBSD): A FEI Scios 2 SEM system equipped with a Hikari Super EBSD Camera, an operating voltage of 20-30 kV, a beam current of 3.2 nA, and a sample working distance of 13-14 mm was used to generate electron backscatter patterns of different points of the

crystals faces. The sample stage was tilted at a 70° angle with respect to the incident electron beam. The cuboid epoxy structure ensured that the sample stage and the exposed crystal faces were parallel to each other. Since the crystals were embedded in an insulating epoxy structure, the side of the epoxy cuboid containing the exposed crystal face was sputter coated with a semi-transparent layer of aluminum (h ~ 6 nm) and grounded using metallic tape for charge dissipation. TEAM™ software tool was used to index obtained backscatter patterns using a Hough transformation-based technique and EBSD maps for a 100-150 μm^2 area were obtained for each crystal facet, with a 1-2 µm steps between indexed points. Although indexing any point in a single crystal would be enough to determine the overall orientation of the crystal, indexing multiple points decreases the uncertainty in the orientation measurement.

D. Picosecond interferometry (PI): Measurements were carried out at room temperature on the indexed faces to measure Brillouin scattering frequencies associated with the orientation of the samples. A train of 785 nm optical pulses were generated by a mode locked Ti:sapphire laser at a repetition rate of ≈ 80 MHz and split into s-polarized pump and p-polarized probe beams. We also employed a two-tint pump-probe setup described previously [24]; i.e., the pump and the probe were also separated spectrally using optical filters. The central wavelength of the probe pulse was 778 nm. The pump beam was modulated at a frequency f = 11 MHz by an electro-optical modulator and its path length was controlled using a mechanical stage. The pump and probe beam were focused to a $1/e^2$ intensity radius w of 5.3 µm on the sample surface at normal incidence through a 10x objective lens. The semi-transparent layer of aluminum sputtered on the facet for EBSD measurements now served as a transducer layer that absorbed pump pulses. The resulting expansion of the Al layer launched an acoustic wave into the crystals. Probe beam reflected at the Al layer and by the moving acoustic wave interfered at the detector leading to Brillouin oscillations in the transient reflectivity signal. Acoustic velocities were calculated from these oscillations as described in the results and discussion section.

III. Results and Discussion

EBSD, PI, and refractive index measurements all require a clean smooth surface, making the polishing process crucial to the rest of the experiment. A poorly polished sample leads to low quality patterns in EBSD. EBSD measurements also require flat sample surfaces, as any tilt inherent in the samples translates into an uncontrolled shift in the angle of incidence. Mounting the irregular crystals in cuboid epoxy structures with parallel faces ensures that the sample surface always lies flat with respect to the stage used in the EBSD measurement. Since the orientation of a crystal is measured with respect to the sample stage, any tilt in the sample relative to the stage will result in an error in the determination of the surface normal. EBSD measurements were not carried out on as-received BP and BAs crystals for this reason, as a normal angle of incidence could not be guaranteed given the irregular shape of the crystals.

Figure 1 summarizes our EBSD measurements for the BP and BAs samples. Crystal orientations extracted from diffraction patterns were fed into the OIM Analysis™ software tool to calculate orientation maps of the exposed faces. The orientation of an exposed crystal face was obtained as the average orientation of all its indexed points. The average orientation spread, which is the average misorientation calculated between each neighboring pair of points, was below 0.4° degree for our BAs samples, below 0.5° for our Si samples, and below 0.7° for our BP samples. For comparison, Wilkinson reported an average spread of 0.5° as the typical uncertainty in an EBSD measurement of a Si single crystal [25].

For anisotropic crystals, the acoustic modes launched normal to the surface in directions other than the high symmetry crystallographic directions are generally not purely longitudinal. The pure longitudinal acoustic waves in the (111) textured Al transducer undergo mode conversion to quasi longitudinal (QL) and quasi shear (QS) modes when crossing into the anisotropic crystals. The longitudinal component of both the QL and QS mode can couple to a probe beam at normal incidence leading to changes in the

transient reflectivity signal [26]. Example measurements of the change in intensity of reflected probe beam versus delay time is shown in fig. 2a.

The smoothly decaying component of the reflected probe intensity (fig. 2a) is due to the cooling of the Al film transducer after excitation by the pump pulse. In this work, we are only interested in the oscillations in the intensity of reflected probe beam that are generated by the propagation of an acoustic pulse in the sample. To subtract the thermal background, the background was fit to an exponentially decaying function and subtracted from the raw data. A Fourier transform of the data with the thermal background subtracted allowed us to find Brillouin scattering frequencies in the data (fig. 2b). Most samples had a single prominent Brillouin frequency, which we attributed to the probe beam reflecting off the QL wave. A secondary mode was observed in one BAs, one Si sample, and two BP samples (fig. 1). We attributed this secondary mode to reflection from QS waves. The amplitude of this secondary mode was studied in the BAs sample and it shows a dependence on the polarization of the probe beam, see fig. S2 in the Supplemental Material [23]. The presence of the secondary mode is also believed to depend on the orientation and quality of the transducer/crystal interface [26]. The latter criterion necessitates a finely polished sample for efficient mode conversion.

Acoustic velocities v were then calculated from the Brillouin frequencies f [27]:

$$v = \frac{\lambda f}{2n}, \tag{2}$$

where λ is the wavelength of the probe beam and n is the refractive index of the material.

We measured the refractive index n at 778 nm of 2.98 ± 0.05 and 3.02 ± 0.06 for BP and BAs, respectively, from our Brewster angle measurements. Our measurement of n for BP, as well as Wettling *et al.*'s [10] values of n over the visible spectra, suggest that n approaches a value 2.98 ± 0.05 in the near-infrared region for BP. Our measurement of n for BAs agrees with recent experiments that

show the refractive index approaching a value of 3.04 ± 0.02 in the near-infrared [28]. A *n* value of 3.69 ± 0.08 was measured for the Si wafer, which is in good agreement with the expected value of *n* = 3.69 [29].

The direction cosines of acoustic waves, along with the elastic constants of a material, can be used to generate Christoffel matrices and solve for velocities of the acoustic waves [30]. Jaeken *et al.* [31] have made a software package available that can construct and solve Christoffel matrices using any given set of elastic constants and for any wave propagation direction and polarization. We modified this package to allow for cycling through a range of possible combinations of elastic constants (C_{11}, C_{12} and C_{44}) and used each combination to calculate quasi longitudinal velocities v_L and quasi shear velocities v_s in the direction normal to the surface of our samples. We then searched for the combination of elastic constants with velocities that best matched the results of our experiments. This was done by calculating a sum of absolute differences ($\Sigma_{\Delta V}$) between measured and calculated longitudinal velocities and $\Sigma_{\Delta V}$ between measured and calculated shear velocities over all samples of each material and all combinations of elastic constants (see fig. 3 for $\Sigma_{\Delta V}$ contour plots of BAs and BP). Any combination with $\Sigma_{\Delta V}$ less than the expected uncertainty in our velocity measurements were chosen as possible set of elastic constants for that material. The uncertainty in the velocity measurements is mostly due to the 2 % uncertainty in measurement of the index of refraction. For the determination of elastic constants from the measured velocities, the uncertainty is further affected by the sensitivity of the velocity in different directions to each of the elastic constants, as well as the total number of velocity measurements for each material.

In cubic crystals, longitudinal velocities are mainly determined by C_{11} and the combination (C_{12} + 2 C_{44}), and only have a slight dependence on C_{12} or C_{44} individually [18,32]. For this reason, $\Sigma_{\Delta V}$ between v_L values were used to solve for the best C_{11} and (C_{12} + 2 C_{44}) values (fig. 3a and 3b). To decouple C_{12} and C_{44}, comparison of $\Sigma_{\Delta V}$ between available v_s values were used along with C_{11} and (C_{12} + 2 C_{44}) values

determined from v_L measurements (fig. 3c and 3d). Since secondary modes (and associated v_s) were not present in all available sample orientations, uncertainty in the individual measurements of C_{12} and C_{44} are high at approximately 18 % and 4 % for C_{12} and C_{44}, respectively. The higher uncertainty in C_{12} than C_{44} suggests that the secondary velocities we measured for BP and BAs were more sensitive to C_{44} than C_{12}. On the other hand, C_{11} and (C_{12} + 2 C_{44}), which were derived from v_L values alone, had a much smaller uncertainty of approximately 2 %.

Using this procedure, we measured C_{11}, C_{12}, and C_{44} values of 165.5 ± 3 GPa, 60 ± 5 GPa, and 81 ± 4 GPa respectively for Si (see fig. S3 in the Supplemental Material [23]). Our measurements for Si are within 2% of accepted values [33].

We found C_{11}, C_{12}, and C_{44} values of 354 ± 5 GPa, 83 ± 15 GPa, and 190 ± 8 GPa for BP and 291 ± 5 GPa, 76 ± 13 GPa, and 173 ± 6 GPa respectively for BAs. The calculated bulk modulus $B_o = (C_{11} + 2\ C_{12})/3$ is 173 GPa for BP and 148 GPa for BAs. Our B_o for BP and BAs are in good agreement with previously reported values of 174 GPa and 148 GPa, respectively [11,13]. The measurements for BP and BAs are summarized in Table I and Table II, respectively.

Previous measurements of elastic constants of BP using Brillouin scattering differ significantly from our measurements, see Table I. Our C_{11} and C_{44} values are 10 % and 15 % higher, respectively, and our C_{12} values are 20% lower than the values measured by Wettling *et al.* [10]. The discrepancy could be the result of the quality of BP crystals available to Wettling *et al.* Transmission electron diffraction patterns of these BP crystal films suggest a crystalline BP growth although the authors commented that the degree of crystallinity varied between samples [12].

Our result for elastic constants of BAs vary by up to 14 % from the values given by Kang *et al.* [15], see Table II. Using C_{11} and (C_{12}+2C_{44}) measured from quasi longitudinal waves in BAs, we derived a longitudinal velocity in the [111] direction $v_{L,111}$ of 8.51 ± 0.13 nm/ps, approximately 4 % larger than the

8.15 ± 0.51 nm/ps value measured by Kang *et al*. [15] using picosecond acoustics (PA). Their smaller $v_{L,111}$ leads to lower C_{11} and (C_{12}+ 2 C_{44}) values and ultimately to an underestimated value for C_{44} that is 14 % smaller than our measurement. Our value for $v_{L,111}$ is within the expected uncertainty of Kang *et al.*'s measurements although the reverse is not true. The PA technique used by Kang *et al.* involves generating acoustic pulse at the sample surface that then travels into the sample. This wave is reflected off the back side of the sample and the echo is detected on the sample surface by a time delayed probe pulse. Kang *et al.* [15] prepared BAs thin films from crystals using focused ion beam machining. Uncertainty in the thickness of this film propagate into uncertainties in the velocity.

Kang *et al*. also measured a surface acoustic wave (SAW) velocity v_{SAW} of 4.32 ± 0.12 nm/ps in the (111) plane of BAs crystals along the [11-2] direction [34]. We used the numerical method described by Li et *al.* [35], along with our measurement of elastic constants, to predict v_{SAW} in the (111) surface of BAs. We calculated v_{SAW} ranging from 4.36 ± 0.15 nm/ps travelling in the [1-10] direction to 4.54 ± 0.13 nm/ps in the [11-2] direction. SAW velocity predicted from our data is 5% larger than what was observed by Kang *et al.*

Table I and Table II also summarize theoretical calculations of elastic constants for BP and BAs obtained using the local density approximation (LDA) exchange-correlation energy functional and the Perdew–Burke–Ernzerhof (PBE) exchange-correlation energy functional. These calculations provide elastic constants at T = 0 K, while the experimental data shown in Tables I and II were acquired at room temperature. Between 0 K and room temperature, we expect the elastic constants of BP and BAs to vary by an amount comparable to the accuracy of our elastic constant measurements. For comparison, experimental data on other zincblende (*ZB*) compounds such as Si and GaAs show that C_{11} changes by 1.1 % and 2.2 %, respectively, between 0 K and room temperature [33,36]. Similarly, C_{44} of Si and GaAs changes by 0.6 % and 2.0 %, respectively [33,36].

Råsander *et al.* [9] reported that, for the 18 semiconductors they considered, calculated values of C_{11} based on either LDA or PBE had an average error of approximately 10 % when compared to experimental measurements. However, PBE approximations to the exchange correlation functional generally underestimated C_{11} whereas the LDA approximations generally overestimated C_{11}. We have compared our measurements with the theoretical values provided by Broido *et al.* [37] and see this trend on BP with the PBE approximations smaller by 4 % and the LDA approximation larger by 2 % than the experimental value. In BAs, the PBE approximation was smaller than experimental value by 8.5 %, but the LDA approximation agreed well with the experimental measurement with a difference of less than 0.5 %.

Råsander *et al.* [9] also reported that LDA is more accurate than PBE, on average, for calculating C_{12} and C_{44}. The average error between measurements and calculations of C_{12} was 9 % and C_{44} was 5 % using LDA, while the average error was 13 % and 10 % for C_{12} and C_{44}, respectively, using PBE. Our measurements of C_{12} and C_{44} were also mostly closer to Broido *et al.*'s [37] LDA calculated values than their PBE calculated ones. For BP, our C_{12} values differed by 12 % and 2 % and C_{44} differed by 2 % and 5 % from values calculated using PBE and LDA, respectively. For BAs, our C_{12} values differed by 15% and 4 % and C_{44} differed by 4 % and 17 % than values calculated using PBE and LDA, respectively. As with estimations of C_{11}, Råsander *et al.* [9] found that the LDA calculated values generally overestimated while the PBE calculated values generally underestimated C_{12} and C_{44}. When comparing against Broido *et al.*'s calculations, our measurements of C_{12} and C_{44} for both BP and BAs were consistently larger than values approximated by PBE calculations. However, our C_{12} and C_{44} values for BAs were both larger than the LDA calculated values while, for BP, the C_{44} value was larger but the C_{12} values was smaller than their LDA calculated counterparts.

Musgrave and Pople [38] related elastic constants of a zincblende (ZB) material to interatomic force constants (IFCs) of a valence force field (VFF) model description of the material. In a VFF model, all

energy changes are expressed in terms of changes of bond lengths and bond angles. This allows for all IFCs to be resolved into bond-stretching and bond-bending forces and the system can be described by using just two force constants—α and β—which are composite functions of all bond stretching and bond bending force constants. Using our measurements, we calculated $\alpha = 77.6$ N/m and $\beta = 30.7$ N/m for BP and $\alpha = 69.7$ N/m and $\beta = 25.7$ N/m for BAs.

Keating [39] and Martin [40] expanded on the use of VFF model to allow for the estimation of bond ionicity in these compounds from their elastic constants. For a perfectly covalent bond:

$$2C_{44}\,(C_{11} + C_{12})/(C_{11} - C_{12})(C_{11} + 3\,C_{12}) = 1. \quad (3)$$

Using our elastic constants for BP and BAs gives a value of 1.02 ± 0.06 and 1.14 ± 0.04 respectively for the left-hand side of equation 3. This suggests that bonds in BP are of slightly higher covalent nature than bonds in BAs crystals. Martin also noted trends between reduced shear moduli $C_{44}^* = C_{44}/C_o$ and $C_s^* = (C_{11} - C_{12})/2C_o$, and nature of bonding in ZB compounds. C_o is defined as $(k_e\, e^2)/r^4$ where k_e is Coulomb's constant and r is the bond length. Using $r = 1.965$ Å for BP and $r = 2.069$ Å for BAs (calculated from lattice parameters [41]), we get $C_{44}^* = 1.23$ and $C_s^* = 0.88$ for BP and $C_{44}^* = 1.38$ and $C_S^* = 0.86$ for BAs. These values are higher than those of Si ($C_{44}^* = 1.08$, $C_S^* = 0.69$) or Ge ($C_{44}^* = 1.06$ and $C_S^* = 0.64$), and closer to diamond ($C_{44}^* = 1.43$ and $C_S^* = 1.18$) than any other material considered by Martin. This is unusual in that the trend of all other binary *ZB* structure compounds considered by Martin suggest decreasing covalent nature of bonding for decreasing C_{44}^* and C_S^* values. One explanation for this anomaly is the presence of boron in BP and BAs. As discussed in Martin's work, the presence of a first-row element leads to more complete s-p hybridization in the compounds, leading to an increase in the reduced shear moduli, similar to what is seen in diamond.

IV. Conclusion

In summary, we report a picosecond interferometry study of high-quality BP and BAs single crystals to determine their elastic constant. We describe our methods to generate and access acoustic waves travelling along different propagation directions in the crystals. We measure C_{11} and C_{12}+2C_{44} with a high degree of precision from quasi longitudinal velocities (error uncertainty below 3 % in all our measurements) and use quasi shear waves to measure individual C_{12} and C_{44} values albeit with larger uncertainties. Our measurements of elastic constants are in good agreement with calculations made using LDA approximations with an average difference of 3 % between measurements and calculated values. Comparisons against values calculated using PBE approximations have a larger average difference of approximately 10 %. Using our measurements in a valence force model (VFF) model of zincblende materials suggests that the bonding in BP is more covalent in nature than the bonding in BAs and that the force constants in BP are larger than in BAs. Our results help assess the accuracy of *ab initio* calculations of the thermal properties of these materials.

Acknowledgements: The authors thank David A. Broido and Chunhua Li for sharing their density functional calculations of elastic constants of BP and BAs. The experiments were carried out in part in the Materials Research Laboratory Central Research Facilities, University of Illinois. This work is supported by Office of Naval Research (ONR) MURI through grant N00014-16-1-2436. The UT Dallas team also would like to acknowledge the support from ONR through grant N00014-19-1-2061.

References

[1] M. M. Waldrop, *The Chips Are down for Moore's Law*, Nature **530**, 144 (2016).

[2] S. V. Garimella, A. S. Fleischer, J. Y. Murthy, A. Keshavarzi, R. Prasher, C. Patel, S. H. Bhavnani, R. Venkatasubramanian, R. Mahajan, Y. Joshi, B. Sammakia, B. A. Myers, L. Chorosinski, M. Baelmans, P. Sathyamurthy, and P. E. Raad, *Thermal Challenges in Next-Generation Electronic Systems*, IEEE Trans. Components Packag. Technol. **31**, 801 (2008).

[3] R. C. Chu, R. E. Simons, M. J. Ellsworth, R. R. Schmidt, and V. Cozzolino, *Review of Cooling Technologies for Computer Products*, IEEE Trans. Device Mater. Reliab. **4**, 568 (2004).

[4] L. Lindsay, D. A. Broido, and T. L. Reinecke, *First-Principles Determination of Ultrahigh Thermal Conductivity of Boron Arsenide: A Competitor for Diamond?*, Phys. Rev. Lett. **111**, 025901 (2013).

[5] Q. Zheng, S. Li, C. Li, Y. Lv, X. Liu, P. Y. Huang, D. A. Broido, B. Lv, and D. G. Cahill, *High Thermal Conductivity in Isotopically Enriched Cubic Boron Phosphide*, Adv. Funct. Mater. **28**, 1805116 (2018).

[6] S. Li, Q. Zheng, Y. Lv, X. Liu, X. Wang, P. Y. Huang, D. G. Cahill, and B. Lv, *High Thermal Conductivity in Cubic Boron Arsenide Crystals*, Science (80-.). **361**, 579 (2018).

[7] J. S. Kang, M. Li, H. Wu, H. Nguyen, and Y. Hu, *Experimental Observation of High Thermal Conductivity in Boron Arsenide*, Science (80-.). **361**, 575 (2018).

[8] D. A. Broido, M. Malorny, G. Birner, N. Mingo, and D. A. Stewart, *Intrinsic Lattice Thermal Conductivity of Semiconductors from First Principles*, Appl. Phys. Lett. **91**, 231922 (2007).

[9] M. Råsander and M. A. Moram, *On the Accuracy of Commonly Used Density Functional Approximations in Determining the Elastic Constants of Insulators and Semiconductors*, J. Chem. Phys. **143**, 144104 (2015).

[10] W. Wettling and J. Windscheif, *Elastic Constants and Refractive Index of Boron Phosphide*, Solid State Commun. **50**, 33 (1984).

[11] V. L. Solozhenko, O. O. Kurakevych, Y. Le Godec, A. V. Kurnosov, and A. R. Oganov, *Boron Phosphide under Pressure: In Situ Study by Raman Scattering and X-Ray Diffraction*, J. Appl. Phys. **116**, 033501 (2014).

[12] S. Yugo and T. Kimura, *Thermoelectric Power of Boron Phosphide at High Temperatures*, Phys. Status Solidi **59**, 363 (1980).

[13] F. Tian, K. Luo, C. Xie, B. Liu, X. Liang, L. Wang, G. A. Gamage, H. Sun, H. Ziyaee, J. Sun, Z. Zhao, B. Xu, G. Gao, X.-F. Zhou, and Z. Ren, *Mechanical Properties of Boron Arsenide Single Crystal*, Appl. Phys. Lett. **114**, 131903 (2019).

[14] R. G. Greene, H. Luo, A. L. Ruoff, S. S. Trail, and F. J. DiSalvo, *Pressure Induced Metastable Amorphization of BAs: Evidence for a Kinetically Frustrated Phase Transformation*, Phys. Rev. Lett. **73**, 2476 (1994).

[15] J. S. Kang, M. Li, H. Wu, H. Nguyen, and Y. Hu, *Basic Physical Properties of Cubic Boron Arsenide*, Appl. Phys. Lett. **115**, 122103 (2019).

[16] B. James, *Acoustic Fields and Waves in Solids, Volumes I and II*, Appl. Acoust. **8**, 72 (1975).

[17] D. Mainprice, *Seismic Anisotropy of the Deep Earth from a Mineral and Rock Physics Perspective*, in *Treatise on Geophysics* (Elsevier, 2007), pp. 437–491.

[18] A. G. Every and W. Sachse, *Determination of the Elastic Constants of Anisotropic Solids from Acoustic-Wave Group-Velocity Measurements*, Phys. Rev. B **42**, 8196 (1990).

[19] H. J. Maris, H. T. Grahn, and J. Tauc, *Nondestructive Evaluation of Thin Film Microstructures by Picosecond Ultrasonics*, MRS Proc. **142**, 39 (1988).

[20] H. B. Huntington, *Ultrasonic Measurements on Single Crystals*, Phys. Rev. **72**, 321 (1947).

[21] B. Lv, Y. Lan, X. Wang, Q. Zhang, Y. Hu, A. J. Jacobson, D. Broido, G. Chen, Z. Ren, and C.-W. Chu, *Experimental Study of the Proposed Super-Thermal-Conductor: BAs*, Appl. Phys. Lett. **106**, 074105 (2015).

[22] E. Hecht, *Optics 2nd Edition*, Addison-Wesley Publishing Company 1987.

[23] *See Supplemental Material at LINK for Additional Details on Measurement of Refractive Indices, Detection of Quasi Shear Waves Using Picosecond Interoferometry, and Determination of Elastic Constans of Si.*, (n.d.).

[24] K. Kang, Y. K. Koh, C. Chiritescu, X. Zheng, and D. G. Cahill, *Two-Tint Pump-Probe Measurements Using a Femtosecond Laser Oscillator and Sharp-Edged Optical Filters*, Rev. Sci. Instrum. **79**, 114901 (2008).

[25] A. J. Wilkinson, *A New Method for Determining Small Misorientations from Electron Back Scatter Diffraction Patterns*, Scr. Mater. **44**, 2379 (2001).

[26] T. Pezeril, P. Ruello, S. Gougeon, N. Chigarev, D. Mounier, J.-M. Breteau, P. Picart, and V. Gusev, *Generation and Detection of Plane Coherent Shear Picosecond Acoustic Pulses by Lasers: Experiment and Theory*, Phys. Rev. B **75**, 174307 (2007).

[27] O. B. Wright, *Thickness and Sound Velocity Measurement in Thin Transparent Films with Laser Picosecond Acoustics*, J. Appl. Phys. **71**, 1617 (1992).

[28] B. Song, K. Chen, K. Bushick, K. A. Mengle, F. Tian, G. A. G. U. Gamage, Z. Ren, E. Kioupakis, and G. Chen, *Optical Properties of Cubic Boron Arsenide*, Appl. Phys. Lett. **116**, 141903 (2020).

[29] M. A. Green and M. J. Keevers, *Optical Properties of Intrinsic Silicon at 300 K*, Prog. Photovoltaics Res. Appl. **3**, 189 (1995).

[30] F. I. Fedorov, *Theory of Elastic Waves in Crystals* (Springer US, Boston, MA, 1968).

[31] J. W. Jaeken and S. Cottenier, *Solving the Christoffel Equation: Phase and Group Velocities*, Comput. Phys. Commun. **207**, 445 (2016).

[32] T. C. T. Ting, *Longitudinal and Transverse Waves in Anisotropic Elastic Materials*, Acta Mech. **185**, 147 (2006).

[33] H. J. McSkimin, *Measurement of Elastic Constants at Low Temperatures by Means of Ultrasonic Waves–Data for Silicon and Germanium Single Crystals, and for Fused Silica*, J. Appl. Phys. **24**, 988 (1953).

[34] Y. Hu, *(Private Communication), School of Engineering and Applied Science, University of California, Los Angeles (UCLA), Los Angeles, California 90095, USA*, (2020).

[35] D. Li and D. G. Cahill, *Attenuation of 7 GHz Surface Acoustic Waves on Silicon*, Phys. Rev. B **94**, 104306 (2016).

[36] R. I. Cottam and G. A. Saunders, *The Elastic Constants of GaAs from 2 K to 320 K*, J. Phys. C Solid State Phys. **6**, 2105 (1973).

[37] D. A. Broido, *(Private Communication), Department of Physics, Boston College, Chestnut Hill, MA 02467, USA*, (2020).

[38] M. J. P. Musgrave and J. A. Pople, *A General Valence Force Field for Diamond*, Proc. R. Soc. London. Ser. A. Math. Phys. Sci. **268**, 474 (1962).

[39] P. N. Keating, *Effect of Invariance Requirements on the Elastic Strain Energy of Crystals with Application to the Diamond Structure*, Phys. Rev. **145**, 637 (1966).

[40] R. M. Martin, *Elastic Properties of ZnS Structure Semiconductors*, Phys. Rev. B **1**, 4005 (1970).

[41] J. A. Perri, S. La Placa, and B. Post, *New Group III-Group V Compounds: BP and BAs*, Acta Crystallogr. **11**, 310 (1958).

[42] H. Meradji, S. Drablia, S. Ghemid, H. Belkhir, B. Bouhafs, and A. Tadjer, *First-Principles Elastic Constants and Electronic Structure of BP, BAs, and BSb*, Phys. Status Solidi Basic Res. **241**, 2881 (2004).

[43] S. Q. Wang and H. Q. Ye, *First-Principles Study on Elastic Properties and Phase Stability of III - V Compounds*, Phys. Status Solidi Basic Res. **240**, 45 (2003).

[44] F. El Haj Hassan, H. Akbarzadeh, and M. Zoaeter, *Structural Properties of Boron Compounds at High Pressure*, J. Phys. Condens. Matter **16**, 293 (2004).

Figures and Tables

TABLE I. Summary of our measurements of the elastic constants of BP compared with results from DFT calculations and past experiments. Uncertainties in the values, when available, are listed in parenthesis next to the values. Elastic constants from Wettling *et al.* [10] were determined by Brillouin scattering; the bulk modulus measurement from Solozhenko *et al.* [11] was determined by X-ray diffraction in a diamond anvil cell. Theoretical values from different sources calculated using either the LDA or PBE exchange correlation energy functionals are also included. The bulk modulus listed for Wettling *et al.*, LDA and PBE calculations, as well as our measurements were calculated from (C_{11}+2C_{12})/3. All experimental data were measured at room temperature, while DFT calculations provide elastic constants at T = 0 K.

	C_{11}(GPa)	C_{12}+2C_{44}(GPa)	C_{12}(GPa)	C_{44}(GPa)	B (GPa)
Our measurements	354 (5)	463 (10)	83 (15)	190 (8)	173
Wettling *et al.* [10]	315 (10)		100 (10)	160 (5)	172
Solozhenko *et al.* [11]					174 (2)
LDA [37]	359.9		81.3	198.9	174.2
LDA [42]	357		87	150	177
LDA [43]	358.9		80.6	196.7	173.4
PBE [37]	339.5		72.8	185.4	161.7
PBE [42]	337		78	200	164
PBE [44]	329		98	154	175

TABLE II. Summary of our measurements of the elastic constants of BAs compared with results from DFT calculations and past experiments. Uncertainties in the values, when available, are listed in parenthesis besides the values. Elastic constants from Kang *et al.* [15] are from picosecond acoustic measurements and were derived, in part, using the bulk modulus reported by Greene *et al.* [14]. Greene *et al.* [14] used x-ray diffraction to obtain the bulk modulus. v_{saw} values listed are for [11-2] direction in the (111) surface of BAs [34]. We calculated v_{saw} from the listed values of elastic constants though a method described by Li *et al.* [35]. Several values calculated using LDA or PBE exchange correlation energy functionals are included. The bulk modulus listed for Kang *et al.*, LDA and PBE calculations, as well as our measurements were calculated from (C_{11}+2C_{12})/3. All experimental data were measured at room temperature, while DFT calculations provide elastic constants at T = 0 K.

	C_{11}(GPa)	C_{12}+2C_{44}(GPa)	C_{12}(GPa)	C_{44}(GPa)	B (GPa)	v_{saw} (nm/ps)
Our measurements	291 (5)	422 (6)	76 (13)	173 (6)	148	4.54 (0.13)
Kang *et al.* [15]	285		79.5	149	148	4.32 (0.12)
Greene *et al.* [14]					148 (6)	
LDA [37]	290.8		73.3	165.6	145.8	
LDA [42]	295		78	177	150	
LDA [43]	291.4		72.8	157.9	145.7	
PBE [37]	266.2		64.7	144.1	131.9	
PBE [42]	275		63	150	134	
PBE [44]	251		80	127	137	

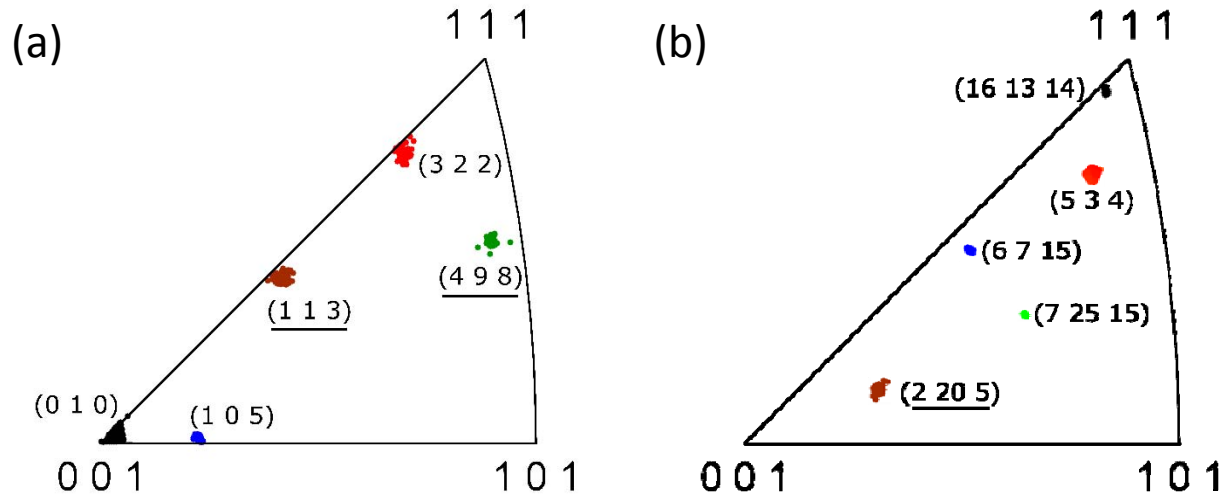

FIG. 1. Summary of EBSD measurements. Inverse pole figures (001) showing all indexed points for (a) BP and (b) BAs crystal faces. Approximately one hundred points over a ~10x10 μm^2 area were indexed from the exposed faces. All indexed points with a good confidence index (CI > 0.1) are shown and points from different faces have been assigned different colors. Average orientation and spread in orientation were calculated for each face. The average orientation of each face is labeled using a *hkl* notation. Orientations where we were able to detect secondary waves are underlined in the figures.

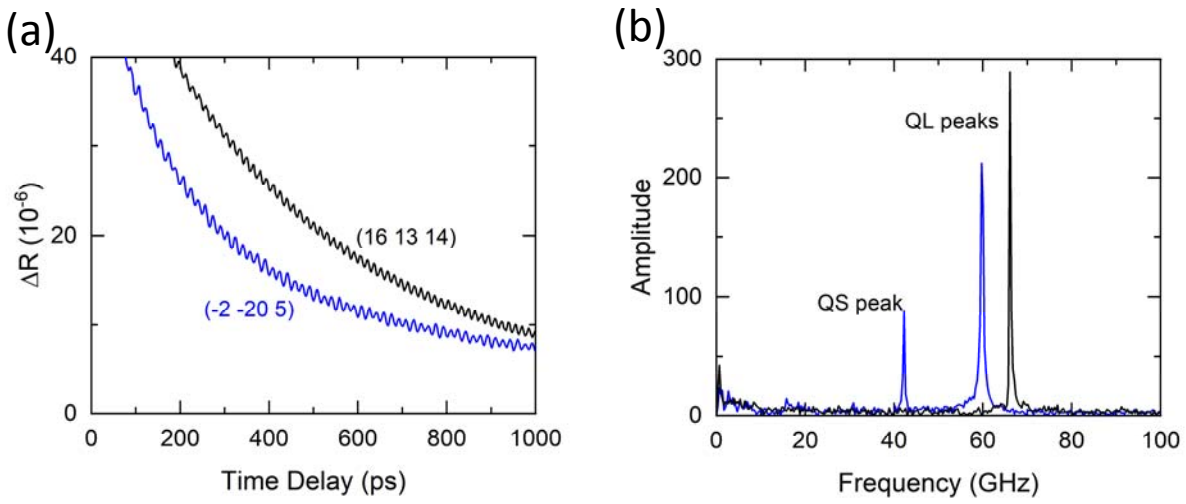

FIG. 2. Picosecond interferometry measurements. (a) Example datasets showing change in reflectivity versus delay time between the probe and the pump pulse for two BAs samples. Both datasets contain Brillouin oscillations from quasi longitudinal acoustic waves (QL) while oscillations from quasi shear (QS) acoustic waves are only present in the (-2 -20 5) dataset. Miller indices (*hkl*) for the crystallographic plane of the probed surfaces are shown. (b) Fourier transformation of the acoustic contributions showing frequencies of Brillouin oscillations present in the datasets from (a).

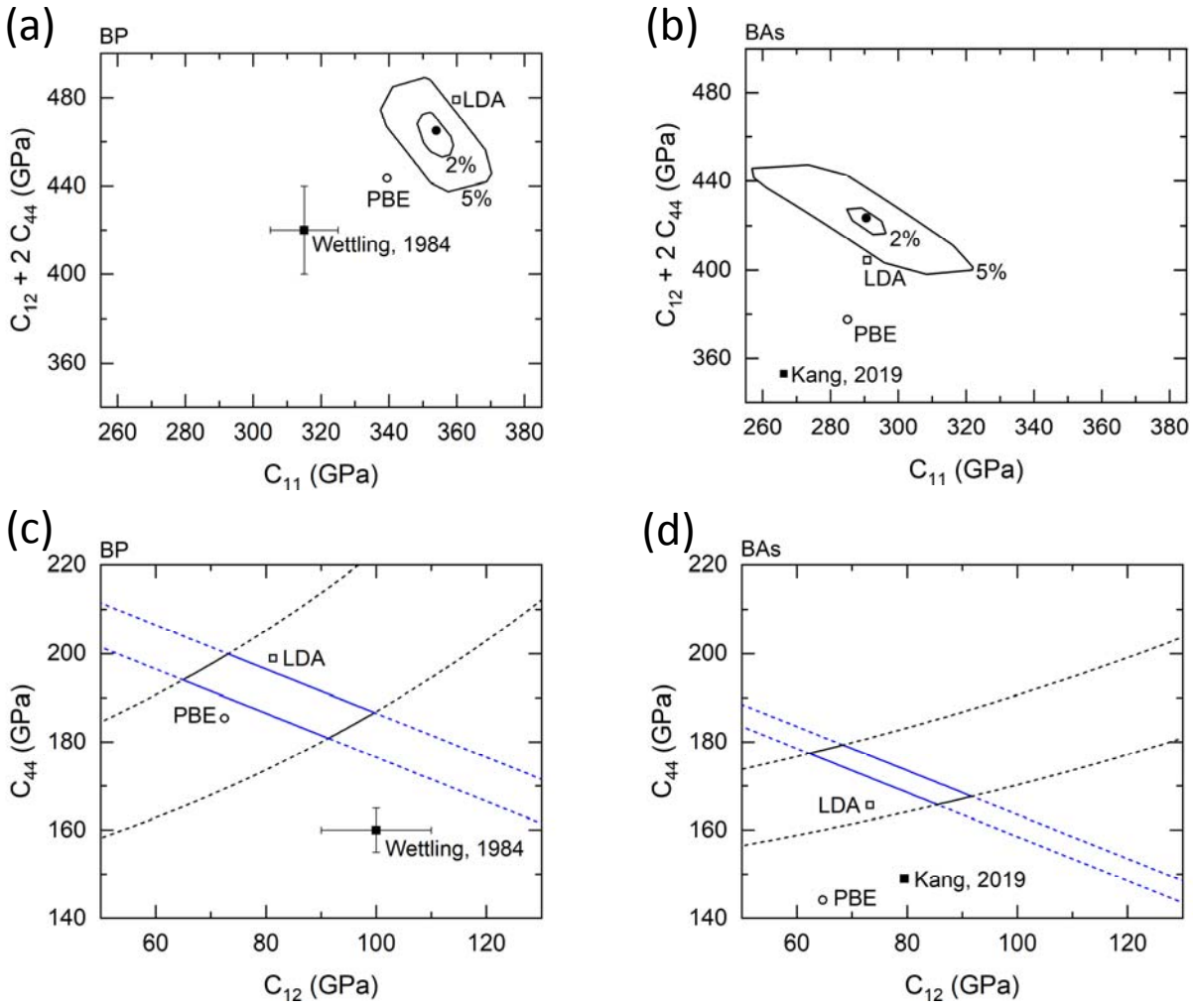

FIG. 3. Summary of elastic constant measurements and comparisons to prior experiments and computational results. Over the range of elastic constant values shown, Christoffel matrices were constructed using elastic constant combination at each point of the plots (step size 0.5 GPa between points) using direction cosines of BP and BAs samples and were solved for quasi longitudinal and quasi shear velocities. (a,b) Contour plots showing sum of absolute differences ($\Sigma_{\Delta V}$) between quasi longitudinal velocities v_L measured using picosecond interferometry vs. v_L calculated using different combinations of C_{11} and C_{12} + 2 C_{44}. The filled circle marks the combination of elastic constants with the lowest $\Sigma_{\Delta V}$ and contour lines for $\Sigma_{\Delta V}$ values of 2% and 5% of average v_L are shown. A 2 % uncertainty is

expected in our velocity measurements, mostly from the uncertainty in our measurements of refractive indices. (c,d) $\Sigma_{\Delta V}$ between measured and calculated quasi shear velocities as a function of C_{12} and C_{44}. C_{11} was held constant at 354 GPa and 291 GPa for BP and BAs respectively for the shear velocity calculations. The blue line encloses the expected value of $C_{12} + 2\ C_{44}$ from v_L measurements, and the area enclosed by the black line include the $\Sigma_{\Delta V}$ values lower than the uncertainty expected in an average shear velocity measurement. Previous experimental values are shown as filled squares [10,15] and values calculated from *ab initio* calculations using local density approximation (LDA) and Perdew, Burke and Ernzerhof (PBE) functionals are included for comparison [37].